This paper is a non-peer reviewed EarthArXiv preprint submitted to AGU Advances

Geodynamic, geodetic, and seismic constraints favour deflated and dense-cored LLVPs

Fred D. Richards[1], Mark J. Hoggard[2], Sia Ghelichkhan[2], Paula Koelemeijer[3,4], & Harriet C.P. Lau[5]

[1]Department of Earth Science & Engineering, Imperial College London, Royal School of Mines, Prince Consort Road, London, SW7 2AZ, UK
[2]Research School of Earth Sciences, Australian National University, 142 Mills Road, Acton, ACT 0200, Australia
[3]Department of Earth Sciences, Royal Holloway University of London, Egham Hill, Egham, TW20 0EX, UK
[4]Department of Earth Sciences, University of Oxford, 3 South Parks Road, OX1 3AN, UK
[5]Department of Earth & Planetary Science, University of California, Berkeley, 307 McCone Hall, Berkeley, CA, 94720, USA

Key Points:

- Observed geoid-to-topography ratio sets effective ∼900 km upper limit on vertical extent of LLVP buoyancy.
- Dynamic topography, geoid, CMB ellipticity, body tides, and Stoneley modes are consistent with dense material in basal 100—200 km of LLVPs.
- This layer is most likely composed of iron- and silicon-enriched crustal material that formed early in Earth's history.

Corresponding author: Fred D. Richards, f.richards19@imperial.ac.uk

Abstract

Two continent-sized features in the deep mantle, the *large low-velocity provinces* (LLVPs), influence Earth's supercontinent cycles, mantle plume generation, and its geochemical budget. Seismological advances have steadily improved LLVP imaging, but several fundamental questions remain unanswered, including: What is the true vertical extent of the buoyancy anomalies within these regions? And, are they purely thermal anomalies, or are they also compositionally distinct? Here, we address these questions using a comprehensive range of geophysical observations. The relationship between measured geoid anomalies and long-wavelength dynamic surface topography places an important upper limit on the vertical extent of long-wavelength LLVP-related density anomalies of ∼900 km above the core-mantle boundary (CMB). Instantaneous mantle flow modelling suggests that anomalously dense material must exist at their base to simultaneously reproduce geoid, dynamic topography, and CMB ellipticity observations. We demonstrate that models incorporating this dense basal layer are consistent with independent measurements of semi-diurnal Earth tides and Stoneley modes. Our thermodynamic calculations indicate that the presence of early-formed, chondrite-enriched basalt in the deepest 100–200 km of the LLVPs is most compatible with these geodynamic, geodetic, and seismological constraints. By reconciling these disparate datasets for the first time, our results demonstrate that, although LLVPs are dominantly thermal structures, their basal sections likely represent a primitive chemical reservoir that is periodically tapped by upwelling mantle plumes.

Plain Language Summary

Images of Earth's deep mantle—constructed by analysing earthquake-triggered waves—reveal two large dome-like regions on top of the core-mantle boundary that slow down such waves. Known as 'large low-velocity provinces' (LLVPs), these enigmatic features are thought to influence fundamental aspects of Earth's evolution, including supercontinent cycles, the distribution of 'hotspot' volcanism, and the stability of the magnetic field. Despite decades of research, key questions around their vertical extent and composition remain unresolved, with studies coming to divergent conclusions depending on the data they use. In this study, we integrate a wide suite of recent geodynamic, geodetic, and seismological observations with numerical modelling to gain a new, unified understanding of LLVPs. We find that they extend no more than 900 km above the core-mantle boundary, that the deepest 100–200 km of these regions contain anomalously dense material, and that this material most likely represents fragments of thick crust that formed early in Earth's history (4 billion years ago) and may have been capped by a meteorite-derived debris layer. These results suggest that, while LLVPs are mainly thermal features, their deepest portions represent a stable, early-formed chemical reservoir that is occasionally sampled by plumes of hot rock ascending from the core-mantle boundary.

1 Introduction

Seismic tomographic models consistently image two large regions of slow seismic velocity in the deep mantle that are widely interpreted to be hotter than ambient material and are spatially correlated with positive, long-wavelength geoid height anomalies (Figures 1 and 2a; Garnero et al., 2016). Early mantle flow studies treated these features as buoyant upwellings and found that an increase of mantle viscosity with depth is required to obtain satisfactory model fits to observed non-hydrostatic geoid height anomalies (Hager et al., 1985; Ricard et al., 1993). Nevertheless, these instantaneous flow calculations are non-unique and suffer from trade-offs between the magnitude and distribution of excess buoyancy. While there is emerging consensus on the lateral extent of LLVPs (e.g., Cottaar & Lekic, 2016), numerous controversies remain concerning their structure and composition.

First, body wave coverage in the mid-to-lower mantle (∼1000–2500 km depth) is limited, with most ray paths traversing this region near-vertically, making global tomographic models susceptible to smearing artefacts in this depth range (Ritsema et al., 2007; Koelemeijer et al., 2018; Maguire et al., 2018). The true vertical extent of thermochemical heterogeneity associated with LLVPs is therefore uncertain, with recent studies suggesting that laterally extensive low-velocity structures imaged at depths ≤2000 km may actually represent tomographic aliasing of clusters of distinct plumes (Davaille & Romanowicz, 2020).

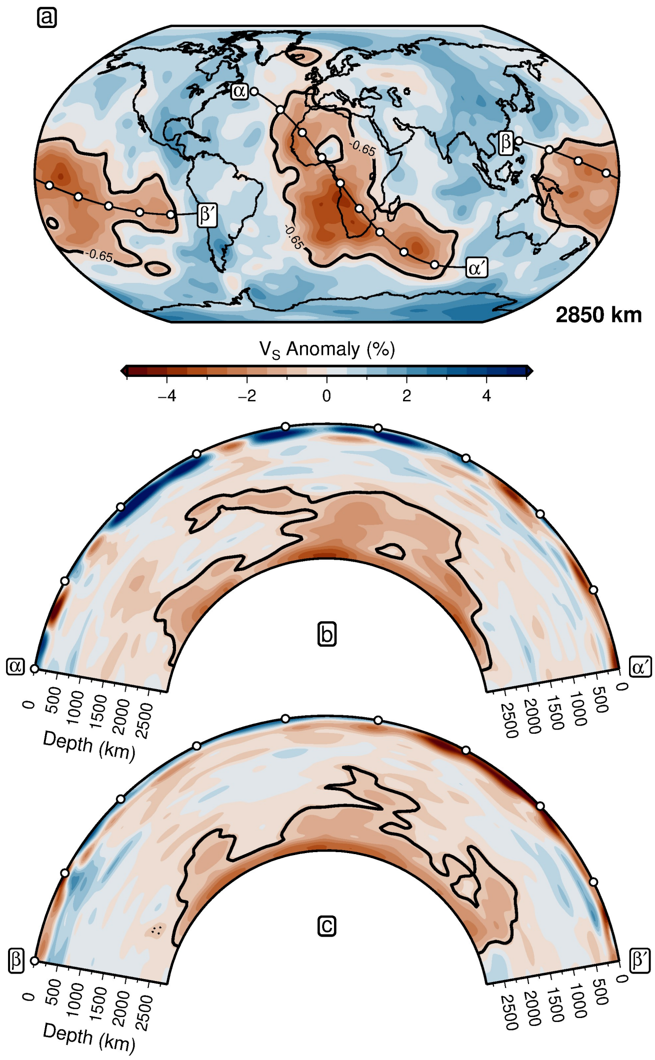

Figure 1. Spatial extent of seismically imaged LLVPs. (a) Shear-wave velocity (V_S) anomalies at 2850 km depth in the TX2011 seismic tomographic model (Grand, 2002), which is used throughout this study. Thick black contour = -0.65% V_S anomaly threshold used to delineate LLVP boundary (Burke et al., 2008); α–α' and β–β' = cross-section locations with white circles spaced at 1000 km intervals. (b) Cross-section α–α' beneath Africa through blended tomographic model (SLNAAFSA above 300 km, TX2011 below 400 km, linearly interpolated between 300–400 km; Schaeffer & Lebedev, 2013, 2014; Celli, Lebedev, Schaeffer, Ravenna, & Gaina, 2020; Celli, Lebedev, Schaeffer, & Gaina, 2020; Hoggard et al., 2020; Grand, 2002). (c) Cross-section β–β' beneath Pacific Ocean.

Second, considerable debate remains over whether LLVPs are purely thermal or also compositionally distinct features. Isotopic variations in intraplate volcanic rocks (Dupré & Allègre, 1983; Hart, 1984; Arevalo Jr et al., 2013), joint seismic-geodynamic inversions (Lu et al., 2020), body tides (Lau et al., 2017), and their apparent stability with respect to the reconstructed locations of Phanerozoic kimberlites and large igneous provinces (Burke et al., 2008), all suggest that LLVPs are enriched in chemically distinct and anomalously dense material. Numerical models suggest that this material must have a $\sim$2–4% intrinsic chemical density excess to generate and preserve such compositional heterogeneity over billion-year timescales (Kellogg et al., 1999; Zhong & Hager, 2003; Tan & Gurnis, 2005; Deschamps & Tackley, 2009; Tan et al., 2011; Tackley, 2012; Y. Li et al., 2014; Mulyukova et al., 2015; Jones et al., 2020). Seismic evidence in favour of chemically distinct LLVPs has, however, proven less conclusive. For example, the decorrelation between shear-wave velocity (V_S) and bulk sound velocity (V_ϕ) below 2000 km depth has been inferred to support both thermal and thermochemical interpretations (Trampert et al., 2004; Della Mora et al., 2011; Moulik & Ekström, 2016; Koelemeijer et al., 2018). Similarly, strong lateral V_S gradients at LLVP boundaries may point to chemical heterogeneity (Ni et al., 2002; Sun & Miller, 2013), but several studies suggest that similar features may occur with purely thermal variations (Schuberth et al., 2009; Davies et al., 2012; Ward et al., 2020). While normal mode studies generally prefer anomalously dense LLVPs (Ishii & Tromp, 2001; Trampert et al., 2004; Moulik & Ekström, 2016), recent Stoneley mode observations (i.e., normal modes trapped along the CMB) indicate that LLVPs are, on average, positively buoyant, although a $\sim$ 100 km-thick, anomalously dense basal layer cannot be ruled out (Koelemeijer et al., 2017). This result apparently contradicts inferences from body tide observations, which yield a mean excess density of $\sim$ 1% within the bottom $\sim$ 350 km of the LLVPs (Lau et al., 2017).

While LLVP buoyancy structure remains uncertain, their morphology and the potential presence of chemically distinct basal material is expected to significantly influence spatiotemporal patterns of mantle circulation (Gurnis et al., 2000; Forte & Mitrovica, 2001; McNamara & Zhong, 2004; Ghelichkhan & Bunge, 2018; M. Li & McNamara, 2018; Lu et al., 2020). Since the earliest models of whole-mantle flow (Hager et al., 1985; Ricard et al., 1993), there have been several important advances in geodynamic observables, notably improved present-day constraints on excess ellipticity of the CMB (Dehant et al., 2017) and the planform of surface dynamic topography (Hoggard et al., 2016). Moreover, recent geodetic and seismological measurements of Earth's long-period motions—in particular, body tides and Stoneley modes—now provide additional bounds on deep mantle density structure. These developments allow us to investigate the trade-off between the magnitude and distribution of LLVP buoyancy, and to re-examine these controversies using new simulations of whole-mantle flow, tidal deformation and Stoneley mode oscillations.

Using a suite of existing tomographic models, we perform geodynamic inversions to determine whether thermal or thermochemical density structures are more compatible with observations of the geoid, CMB ellipticity, and dynamic topography. The best-fitting density configurations are then tested against independent Stoneley mode splitting and body tide measurements, and we demonstrate that the existing discrepancies between these datasets can be resolved. Finally, we explore geochemical implications of these inversion-derived buoyancy structures using thermodynamic calculations of density and elastic properties of possible compositional endmembers. By analysing the fits of the resulting model predictions with a wide range of observations, we constrain the nature and distribution of chemical heterogeneity within the deep Earth.

2 Reconciling geodynamic observations and predictions

Recent re-evaluation of dynamic surface topography using global inventories of residual depth measurements confirms that the long-wavelength component of this field is spatially correlated with geoid height anomalies (Figure 2a–b; Hoggard et al., 2016, 2017). While

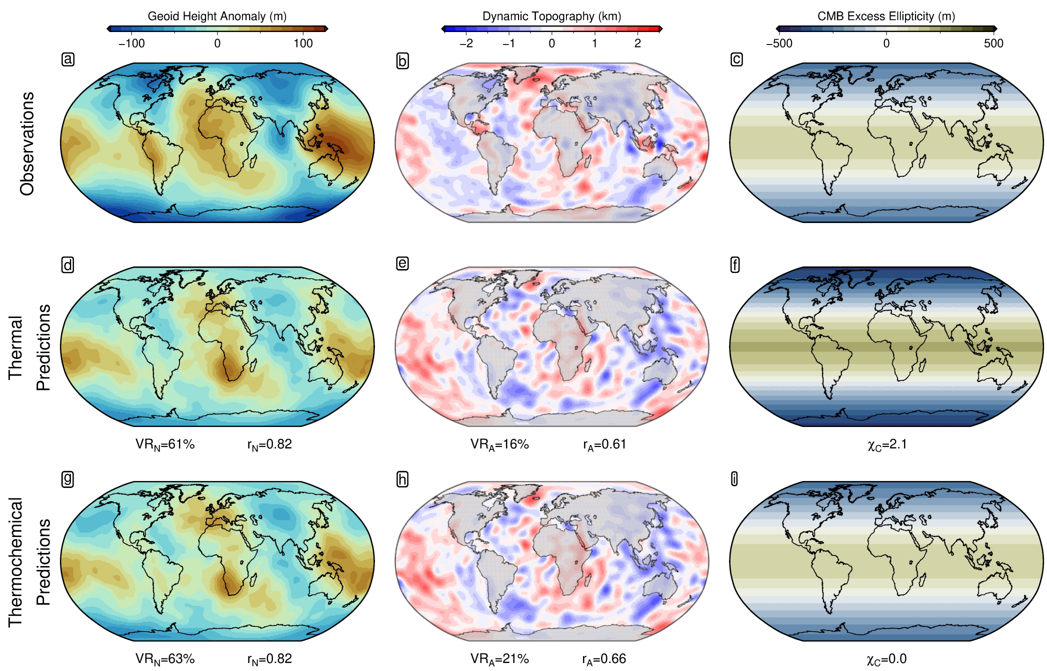

Figure 2. Observations versus optimal instantaneous flow modelling predictions for TX2011 tomographic model and S10 viscosity profile. (a) Observed non-hydrostatic geoid height anomalies (Förste et al., 2008; Chambat et al., 2010). (b) Observed dynamic surface topography (Hoggard et al., 2017). (c) Observed excess CMB ellipticity (Dehant et al., 2017). (d) Predicted geoid for optimal mantle density model assuming LLVPs are purely thermal features. VR = variance reduction; r = Pearson's correlation coefficient (Appendix C). (e) Predicted dynamic topography for this model. (f) Predicted excess CMB ellipticity for this model. χ_C = misfit to observed CMB excess ellipticity (Appendix C). (g–i) Same for optimal density model that includes compositionally distinct LLVPs.

there is some disagreement on the appropriate methodology for spectrally analysing these data, studies have converged on water-loaded amplitudes of $\pm$700 m at spherical harmonic degrees l = 1–3 (Hoggard et al., 2016; Yang & Gurnis, 2016; Watkins & Conrad, 2018; Davies et al., 2019; Steinberger et al., 2019; Valentine & Davies, 2020). Meanwhile, for its core-mantle boundary counterpart, geodetic observations of Earth's free core nutation place a narrow bound of $\sim 400 \pm 100$ m on the amplitude of the degree-two ($l = 2$), order-zero ($m = 0$) component of non-hydrostatic CMB topography (i.e., excess ellipticity; Figure 2c; Dehant et al., 2017). Unfortunately, efforts to map global CMB topography at shorter wavelengths using seismic data are presently hampered by trade-offs between velocity and density structure in the D$''$ region (Koelemeijer, 2021).

In light of these improved and revised constraints, we ask: Can a model of V_S-derived mantle density be constructed that simultaneously satisfies the geoid, dynamic topography, and excess CMB ellipticity? To investigate this issue, we construct a suite of $\sim 10^6$ density models, simulate the resulting instantaneous mantle flow, and compute misfits to the observational data sets (Appendices A–C). For the upper mantle above 400 km, we adopt a modified version of the RHGW20 density model (F. D. Richards et al., 2020), which accounts for anelasticity at seismic frequencies and yields demonstrably better fit to short-wavelength dynamic topography than previous models. We divide the deeper mantle into five layers, and within each layer, we vary the V_S-to-density scaling factor ($R_\rho = \frac{\mathrm{d}\ln\rho}{\mathrm{d}\ln V_S}$) between 0.1–

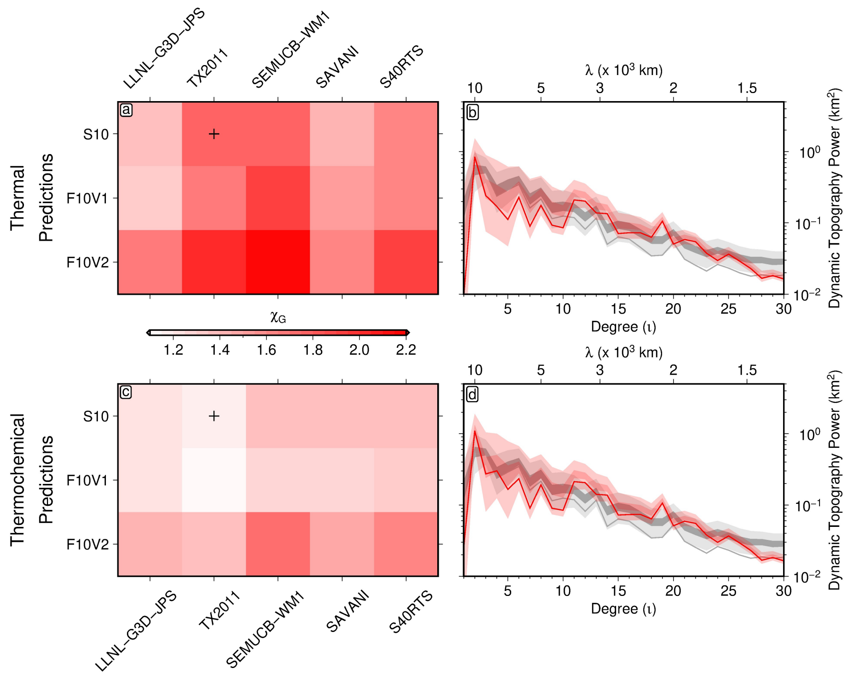

Figure 3. Geodynamic misfit as a function of input density and viscosity model. (a) Total geodynamic misfit, χ_G (Appendix C), of best-fit thermal models for each combination of viscosity and seismic tomographic input. Black cross = model shown in (b) and Figure 2d–f. (b) Observed and predicted dynamic topography power spectra of best-fit thermal model for TX2011 and S10 viscosity profile. Dark and light gray envelope = 99% and 50% confidence intervals for power spectrum of optimal spherical harmonic coefficients for oceanic residual depth measurements (intervals derived from 100,000 random samples of inverted spherical harmonic coefficient probability distributions; Valentine & Davies, 2020); solid gray line = power spectrum of mean spherical harmonic coefficients determined for oceanic residual depth measurements; dark and light red envelope = 99% and 50% confidence intervals for power spectrum of thermal model constructed by sampling predicted dynamic topography at locations of shiptrack and point-wise oceanic residual depth measurements and determining optimal spherical harmonic coefficients using Gaussian process-based methodology of Valentine & Davies (2020); solid red line = power spectrum of mean spherical harmonic coefficients determined for thermal model. (c) Total geodynamic misfit, χ_G, of best-fit thermochemical models for each combination of viscosity and seismic tomographic input. Black cross = model shown in (d) and Figure 2g–i. (d) Observed and predicted dynamic topography power spectra of best-fit thermochemical model for TX2011 and S10 viscosity profile, as in (b).

0.4. This range is in line with expectations from mineral physics constraints on pyrolitic and mixed pyrolitic-basaltic compositions, which are both hypothetical compositions for an isochemical mantle (Deschamps et al., 2012; Stixrude & Lithgow-Bertelloni, 2012; Lu et al., 2020). To allow for limited seismic resolution and potential imaging artefacts in the lower mid-mantle (1000–2000 km), we also test $R_\rho = 0$ in this region. In addition to using models with vertically varying V_S-to-density scaling factors, we construct a suite of thermochemical models where chemical heterogeneity is represented as a density jump, ranging between 0.0–2.0%, between the LLVP interior and exterior. We generate density models using five seismic tomographic models and perform instantaneous flow calculations using three mantle viscosity profiles (Appendices A and B).

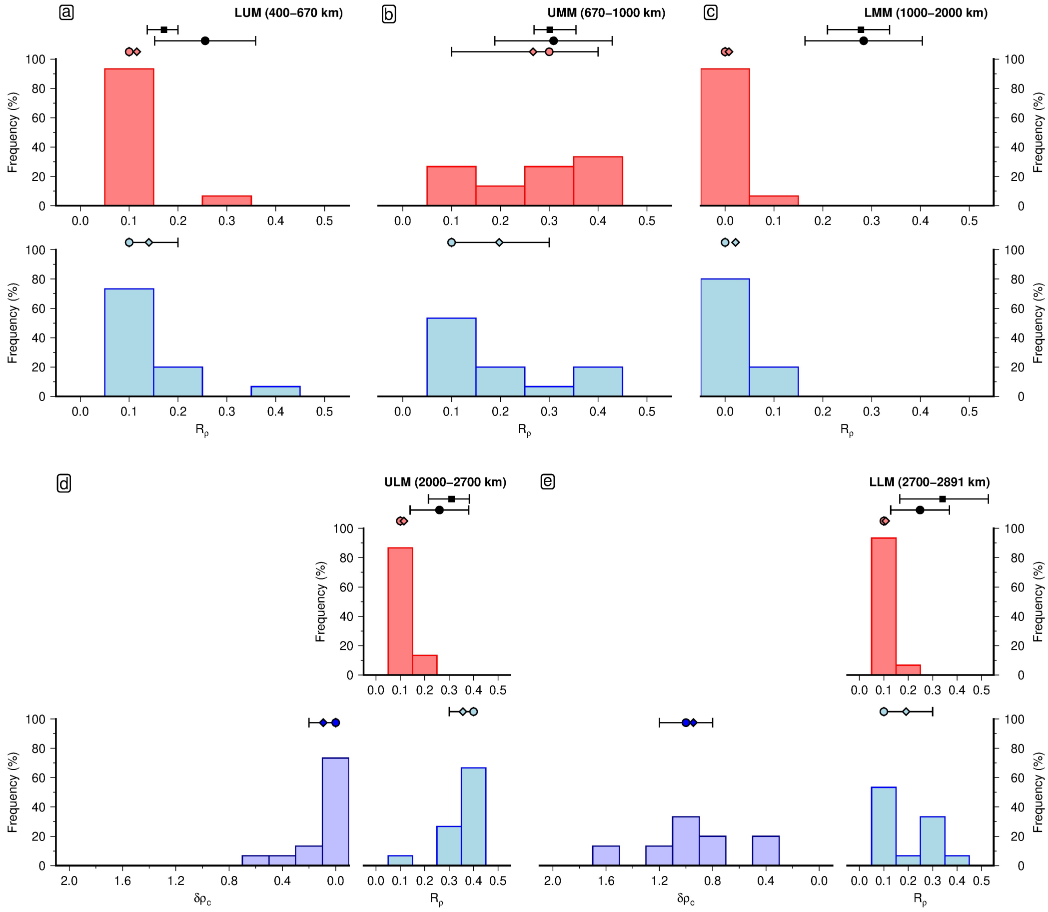

Figure 4. Best-fitting R_ρ values for thermal and thermochemical models. (a) Lower upper mantle layer (400–670 km). Red bars = best-fitting R_ρ for thermal models; blue bars = best-fitting R_ρ for thermochemical models; coloured circles and error bars = medians and interquartile ranges; diamonds = mean weighted by total misfit, χ_G; black circle and error bars = predicted values and $\pm 2\sigma$ errors for a pyrolitic mantle composition, excluding post-perovskite (taken from Lu et al., 2020); black square and error bars = predicted values and $\pm 2\sigma$ errors for mantle compositions ranging from a mechanical mixture of 50% MORB and 50% pyrolite to 100% pyrolite, determined using Perple_X (Connolly, 2005; Stixrude & Lithgow-Bertelloni, 2011). In both cases, thermodynamic R_ρ predictions are corrected for anelasticity following methodology outlined in Lu et al. (2020) and Text S2.2. (b) Same for upper mid-mantle layer (670–1000 km). (c) Same for lower mid-mantle layer (1000–2000 km). (d) Same for upper lower mantle layer (2000–2700 km). Dark blue bars = best-fitting compositional density contrast, $\delta\rho_c$, for thermochemical models. (e) Same for lower lower mantle layer (2000–2700 km).

Three key results emerge from this analysis. First, we find that acceptable fits to both the geoid and dynamic surface topography can be obtained for thermal and thermochemical density models (Figures 2, 3, and S1–S6; Table S1). Second, we obtain lower misfits, higher correlation coefficients, and greater variance reductions for models that include compositionally distinct material in the LLVPs relative to purely thermal models (Appendix C). This difference is particularly clear for the excess CMB ellipticity (Figure 2f versus 2i). Thermochemical models generally prefer strong excess density within the LLVP portion of the D″

layer ($\delta\rho_c \geq +0.8\%$ for 13 of 15 tomographic and viscosity model combinations), but find little to no excess density in the shallower 2000–2700 km depth range ($\delta\rho_c \leq +0.2\%$ for 13 of 15 models; Figure 4d and 4e; Table S3). The thermochemical models also generally return R_ρ values throughout the middle (400–1000 km) and lower (2000–2900 km) mantle that are in better agreement with experimental expectations for a pyrolitic composition (Figure 4a, 4b, 4d and 4e; Deschamps et al., 2012; Lu et al., 2020). Third, all best-fitting models require $R_\rho \sim 0$ for the 1000–2000 km mid-mantle layer, irrespective of whether or not LLVP regions are modelled as compositionally distinct (Figure 4c; Tables S2–S3; for more discussion see Text S1.1–1.2).

3 Vertical extent of LLVPs

The geodynamic inversions exhibit a preference for $R_\rho \sim 0$ throughout the mid-mantle, which is too low for any plausible mantle composition and indicates that geodynamic observables are incompatible with strong thermal buoyancy contributions from this depth. Given that seismic tomographic models are dominated by $l = 2$ structure over the 1000–2000 km depth range, we explore this result further using associated sensitivity kernels for instantaneous mantle flow.

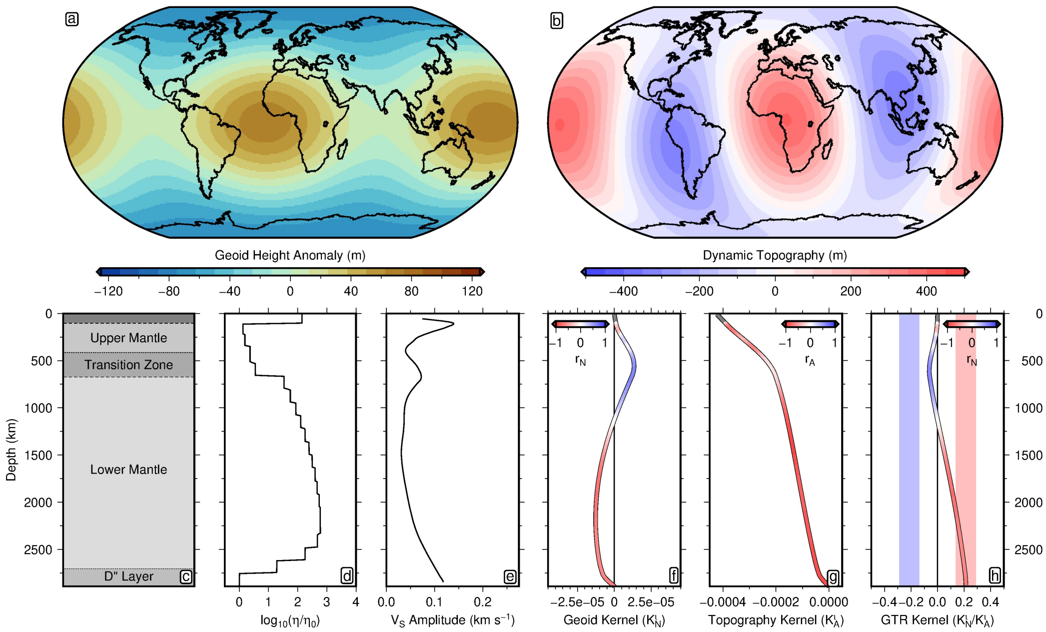

Figure 5. Relationship between degree-two dynamic topography, geoid and V_S anomalies. (a) Observed non-hydrostatic geoid height anomalies (Förste et al., 2008; Chambat et al., 2010). (b) Observed water-loaded dynamic topography (Davies et al., 2019). (c) Schematic radial mantle structure. (d) Normalised radial viscosity, η, profile (S10; Steinberger et al., 2010). (e) Spectral amplitude of $l = 2$ V_S anomalies from SEMUCB-WM1 tomographic model (French & Romanowicz, 2015). (f) Geoid kernel, K_N^l, coloured by geoid-to-V_S anomaly correlation, r_N, as a function of depth. (g) Dynamic topography kernel, K_A^l, coloured by dynamic topography-to-V_S anomaly correlation, r_A. (h) Geoid-to-topography ratio (GTR) kernel, coloured by r_N. Blue/red bands = values required to produce the observed GTR when thermal density anomalies are correlated/anti-correlated with the geoid.

The geoid-to-topography amplitude ratio (GTR) at $l = 2$ provides a crucial constraint on the vertical extent of long-wavelength buoyancy anomalies associated with LLVPs. In Figures 5a and b, we show the $l = 2$ components of observed non-hydrostatic geoid height anomalies and water-loaded dynamic topography, which yield an estimated GTR of $\sim 0.21 \pm 0.07$. These deflections must be caused by $l = 2$ density anomalies, with the strongest corresponding shear-wave velocity (V_S) anomalies found within the LLVP regions, the mantle transition zone, and the asthenosphere (Figure 5e). These V_S anomalies are anti-correlated with the observed geoid and dynamic topography, with the exception of the transition zone, where V_S anomalies correlate with the geoid but remain anti-correlated or become decorrelated with dynamic topography (Figure 5f–g).

Individual $l = 2$ sensitivity kernels for the geoid, dynamic topography, and GTR (Figure 5f–h; Appendix B) are sensitive to the choice of mantle viscosity profile (Figure 5d), but their shape is broadly consistent for a range of published profiles (Figure S8; Forte et al., 2010; Liu & Zhong, 2016). The $l = 2$ GTR kernel shows that, to satisfy the observed value of 0.21 ± 0.07, density anomalies must either anti-correlate with surface deflections in the deep mantle (intersection with red band in Figure 5h) or positively correlate with the geoid—while remaining negatively correlated with dynamic topography—in the transition zone (intersection with blue band in Figure 5h). Our analyses support the conclusions of previous studies (e.g., Hager et al., 1985) that deeper mantle structure is the dominant contributor to the integrated GTR. These kernels also show that any $l = 2$, mid-mantle ($\sim$1000–2000 km) thermal density anomalies can only lower the GTR. A mantle density model with LLVPs extending shallower than $\sim$2000 km depth (i.e., sim900 km above the CMB) that fits the observed geoid will therefore inevitably overpredict long-wavelength dynamic topography. Hence, the inversions return a preferred value of $R_\rho \approx 0$ in the mid-mantle. This finding provides strong evidence that long-wavelength low density anomalies associated with LLVPs do not vertically extend beyond 900 km above the CMB, which is consistent with recent arguments that seismically imaged $l = 2$, mid-mantle V_S structure is an artefact of limited tomographic resolution (Davaille & Romanowicz, 2020). Smaller scale density anomalies do exist in the 1000–2000 km depth interval (e.g., plumes and slabs; French & Romanowicz, 2015; N. Simmons et al., 2015); however, instantaneous flow sensitivity kernels for shorter wavelengths approach zero over this depth range, such that these features have minimal impact on the geoid, surface dynamic topography and CMB ellipticity. Indeed, geodynamic misfit changes by less than 10% when our optimised density fields are modified to suppress $l = 2$ structure while retaining shorter wavelength features between 1000–2000 km depth (by instead applying a high-pass filter and setting $R_\rho = 0.2$, see Text S1.3; Karato & Karki, 2001).

4 Compatibility with body tides and Stoneley modes

Despite similar, though not completely identical sensitivity to deep Earth structure (Robson et al., 2022), previous studies based on semi-diurnal body tide and Stoneley mode splitting observations arrive at contrasting conclusions about LLVP density structure. The former show a clear preference for the presence of anomalously dense material, with trade-offs between the amplitude and depth distribution of excess density (Lau et al., 2017). In contrast, by also taking topography of the CMB into account, the latter prefer models with integrated density anomalies in the lower 400 km that are negative, as expected for a dominantly thermal control (Koelemeijer et al., 2017). In light of these studies, we next test whether the mantle structure obtained from our optimal TX2011-based geodynamic model with thermochemical variations, or its purely thermal counterpart, is most consistent with these geodetic and seismological observations.

Goodness-of-fit to semi-diurnal body tide constraints is calculated following the methodology of Lau et al. (2017), which requires the improvement of predictions for 3D mantle structure over a 1D reference case to be significant at the 95% level (Appendix D). The optimal TX2011-derived thermal model produces results that are only significant at the 93.8%

level. By contrast, the best-fitting thermochemical density model based on the same tomographic input, but with chemical heterogeneity in the base of LLVPs, yields statistically significant outcomes (95.8% significance level).

We predict Stoneley mode splitting functions by adapting the methodology of Koelemeijer et al. (2017) (Appendix D). Our revised approach has two methodological advantages over this study. Firstly, both the range and magnitude of R_ρ tested here are consistent with candidate chemical compositions in the deep mantle (as compiled by Lu et al., 2020). Secondly, by calculating the instantaneous mantle flow associated with each model, CMB deflections are dynamically consistent with each LLVP density structure rather than scaled. We find that the misfit between observed and predicted Stoneley mode splitting functions is $\sim$20% lower for the optimal TX2011-based thermochemical density model compared with its equivalent thermal model (Table S4; Figure S9). This conclusion appears to contradict the findings of Koelemeijer et al. (2017), but is readily explained by our methodological improvements, as well as the stronger V_S amplitudes at $l = 2$ below 2500 km depth in TX2011 compared to the SP12RTS model adopted in that study (Text S1.4).

Significantly, these results indicate that the presence of anomalously dense material in the bottom $\sim$200 km of the LLVPs is not only compatible with available geodynamic constraints, but is also consistent with observations of Earth's semi-diurnal body tide and Stoneley mode splitting.

5 Implications for lower mantle chemistry

Having established that geodynamic, seismological, and geodetic constraints provide evidence for the presence of a dense basal layer within the LLVPs, we explore the compatibility of different candidate compositions. Several hypotheses have been proposed for the formation of chemically distinct LLVP material, including: slow accumulation of basalt from subducted slabs reaching the CMB (Niu, 2018); preservation of primordial mantle material segregated during top-down crystallisation of a basal magma ocean (Labrosse et al., 2007); subduction of iron- and silicon-rich Hadean crust along with a terrestrial regolith comprising chondritic and solar–wind-implanted material (Tolstikhin & Hofmann, 2005); and pooling of dense, iron-rich melts generated in the primordial mantle transition zone (Lee et al., 2010).

We have assembled three endmembers to test the compositional range encompassed by these different scenarios: i) present-day mid-ocean ridge basalt (MORB; lowest iron, highest silicon content; Workman & Hart, 2005); ii) chondrite-enriched Hadean basalt (intermediate iron and silicon; Tolstikhin & Hofmann, 2005); iii) iron-enriched pyrolite (highest iron, lowest silicon), representing early Archaean melts generated in the transition zone or remnants of a basal magma ocean (Lee et al., 2010; Labrosse et al., 2007; Table A1; for more discussion see Text S2.1–2.2). For each of these compositions, we perform thermodynamic modelling and find that all options yield a positive density and negative shear-wave velocity anomaly with respect to ambient pyrolitic mantle at deep mantle temperatures and pressures ($\sim$ 2000–4000 K; $\sim$ 110–140 GPa; Figure S10; Connolly, 2005; Stixrude & Lithgow-Bertelloni, 2011). The amplitude of these anomalies vary, with modern basaltic material generating the weakest anomalies, while the most iron-rich primordial components produce the strongest anomalies (Workman & Hart, 2005; Lee et al., 2010).

The relatively modest excess density below 2700 km recovered in our initial geodynamic inversions ($\overline{\delta\rho_c}$ =0.4–1.6%) is consistent with mechanical mixtures comprising 20–70% pyrolite and 80–30% modern MORB, or 50–90% pyrolite and 50–10% of either iron-rich primordial component. This excess density, however, falls below the $\sim$2–4% threshold required for long-term preservation of intra-LLVP chemical heterogeneity (Tackley, 2012; Mulyukova et al., 2015; Jones et al., 2020). We therefore explore how a trade-off between the thickness of the basal layer and its excess density affects the fit to the geodynamic and seismic constraints, and which of the proposed chemical compositions are most compatible.

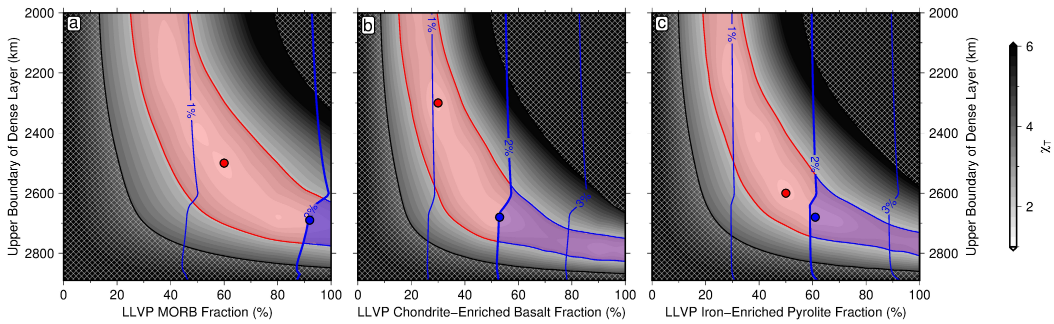

Figure 6. Combined misfit to geodynamic and Stoneley mode observations as a function of mantle composition. (a) Combined total misfit (χ_T) as a function of MORB fraction within the LLVPs (Workman & Hart, 2005). Material outside the LLVPs is assumed to be pyrolitic. Hatched region = models with peak-to-valley l = 2 CMB topography exceeding ±4.7 km maximum constraint (Koelemeijer, 2021); red circle = best-fitting model; red shading = models with misfit less than double that of global minimum; thin blue contours = compositional density difference between dense layer material and ambient mantle; bold blue contour = lower limit of suggested ∼2–4% compositional density threshold for long-term preservation of intra-LLVP chemical heterogeneity (Tackley, 2012; Mulyukova et al., 2015; Jones et al., 2020); blue circle = best-fitting model with intrinsic density anomaly above preservation threshold; blue shading = models with misfit less than double that of global minimum and compositional density anomaly above preservation threshold. (b) Same for primordial material (chondrite-enriched basalt; Tolstikhin & Hofmann, 2005). (c) Same for primordial material (iron-enriched pyrolite; Lee et al., 2010).

Instantaneous flow calculations are repeated with density models constructed from the thermodynamic predictions for different combinations of chemical components within and outside the LLVPs (Appendices A and B). Mantle material is modelled as a mechanical mixture of pyrolite and each candidate composition, with density anomalies set to zero between 1000–2000 km depth based on the geodynamic inversion results. We find a strong trade-off between the anomalous density of the basal LLVP region and its thickness, with similar misfit to geodynamic observables obtained for thin, highly enriched versus thicker, less chemically distinct basal layers (Figure S16). Although results are dependent on the radial mantle viscosity profile, optimal fits are generally obtained for thinner, more enriched layers, irrespective of whether anomalously dense material within the LLVPs is assumed to be basaltic or primordial. Best-fitting models for each chemical component yield similar misfit values, with optimal layer thicknesses of ∼200 km.

Combining geodynamic and Stoneley mode misfit into a joint misfit function does not significantly reduce the trade-off between basal layer thickness and density (Appendix D; Figures S12, S13, and S15). Nevertheless, while each endmember composition can generate density models that satisfy the 2–4% excess density threshold for long-term chemical heterogeneity preservation (Tackley, 2012; Mulyukova et al., 2015; Jones et al., 2020), the two primordial candidates yield a ∼ 10% reduction in joint misfit to Stoneley mode and geodynamic observations compared with recycled MORB (Figure 6). Irrespective of whether the `TX2011` or `S40RTS` tomographic model is used to generate density structure, optimal chondrite-enriched basaltic configurations give ∼5–10% lower misfit than their iron-enriched pyrolitic counterpart, indicating that a 100–200 km-thick layer, mainly composed of sequestered Hadean crust, is most consistent with available data (Text S2.3; Figures 6 and S13–S15).

Although the uncertainty inherent to thermodynamic estimations of V_S and density means that our conclusion regarding basal layer composition is not definitive (Connolly & Khan, 2016), the presence of Hadean crust in these regions is consistent with several independent constraints. Firstly, time-dependent thermochemical convection studies suggest that subducted, $\sim$ 10 km-thick present-day oceanic crust is easily re-entrained, whereas an early-formed proto-crust with greater thickness and higher iron content could be more readily preserved within the base of LLVPs (M. Li & McNamara, 2013; M. Li et al., 2014). Secondly, the elevated SiO_2 content of the primordial basaltic composition compared with iron-enriched pyrolite helps to explain the observed spatial decorrelation between V_ϕ and V_S in the lowermost mantle, provided that bridgmanite is at least partially replaced by post-perovskite within this depth range (Su & Dziewonski, 1997; Hernlund & Houser, 2008; Koelemeijer et al., 2018; Figure S10). Thirdly, the less extreme reduction in V_S at lowermost mantle conditions for primordial basalt ($\sim$ 2%), compared to iron-enriched pyrolite ($\sim$ 3%), is more compatible with the relatively modest V_S gradients that have been inferred across LLVP boundaries (Hernlund & Houser, 2008; Davies et al., 2012; Deschamps et al., 2012; Ward et al., 2020). Finally, when comparing observed and predicted V_S, V_P and V_ϕ signatures for a wide range of candidate LLVP compositions, Vilella et al. (2021) found that seismic constraints necessitate minimal quantities of ferropericlase (<6 vol%) and potentially large proportions of calcium-perovskite (up to $\sim$35 vol%), consistent with expected phase assemblages for basaltic material at deep mantle conditions. Optimal compositions found by this study also feature elevated Al_2O_3 contents (3–13 wt%) and oxidation states ($Fe^{3+}/\sum Fe > 0.3$), which can be attributed to the addition of chondritic material and chemical partitioning during a shallow melting event (McKay et al., 1991; Walter, 1998; Zega et al., 2003; Herzberg, 2016; Zhang et al., 2017; Table A1).

For all the reasons listed above, we conclude that the most likely candidate for the chemically distinct, 100–200 km-thick basal layer is Hadean basaltic material combined with solar wind-implanted chondritic regolith (Tolstikhin & Hofmann, 2005). Nevertheless, more iron-rich and silicon-poor primordial endmembers, or mixtures of these components, cannot currently be discounted given the uncertainties associated with lower mantle seismic tomographic imaging, viscosity structure, and the inference of physical properties from seismic observations. We also note that the geodynamic, seismological, and geodetic constraints we use here are only sensitive to long-wavelength density variations. As a result, the dense material we identify may be unevenly distributed within the basal layers and potentially concentrated beneath broad thermochemical plumes (e.g., Davaille & Romanowicz, 2020; Lu et al., 2020).

Sites of past and present intraplate volcanism have been shown to spatially correlate with LLVPs, leading to speculation that anomalous isotope ratios of basalts erupted in these settings may originate from these deep mantle reservoirs (Hart, 1984; Castillo, 1988; White, 2015). These isotopic signatures include high He^3/He^4 ratios and positive $\mu^{182}W$ anomalies. Since all He^3 is of primordial origin and the decay of ^{182}Hf to ^{182}W has a half-life of only $\sim$ 9 Myr, these chemical signals point to the presence of an early-formed and largely isolated (i.e., relatively undegassed) geochemical reservoir. Our finding that the basal $\sim$100–200 km of the LLVPs most likely contain iron- and silicon-enriched primordial material, rather than accumulations of more youthful MORB, suggests that these regions are the source of these anomalies and that additional geochemical deviations are therefore derived from other reservoirs (Mundl-Petermeier et al., 2020; Gleeson et al., 2021; Day et al., 2022; Tucker et al., 2022). This inference is further supported by the agreement between the approximate mass of these layers ($3 - -6 \times 10^{22}$ kg) and that of the primordial Earth reservoir inferred from He^3/He^4 ratios ($\sim 6.2 \times 10^{22}$ kg; Tolstikhin & Hofmann, 2005). Finally, our finding that LLVP basal layers likely contain chondrite-enriched basalt, coupled with their relative thinness, is also consistent with geodynamic studies investigating the origin of systematic $\mu^{182}W$ differences between ocean island basalts and flood basalts erupted in large igneous provinces (Jones et al., 2019). Clearly further integration of geochemical and geophysical constraints is needed to confirm whether these thin basal layers represent Hadean crust, remnants of magmatic processes within the early Earth's interior, or a combination of both. Our proposed model of Earth structure does, however, already provide a self-consistent explanation of a full range of geodynamic, geodetic, seismological, and geochemical constraints.

Both the presence of dense primordial material within LLVPs and the limited vertical extent of their associated buoyancy (≤ 900 km above the CMB) have important implications for existing predictions of mantle evolution, reducing the amplitude and slowing the rate of change of surface dynamic topography. By adopting this structure and validating its associated mantle flow field against evidence for continent-scale uplift and subsidence encoded in the geological record, our understanding of Earth's internal dynamics can be greatly refined, allowing impacts on landscape evolution and palaeoclimatic shifts to be determined with unprecedented fidelity.

6 Conclusions

Determining the thermochemical properties and vertical extent of LLVP-related buoyancy anomalies is of fundamental importance to solving a range of outstanding controversies in Earth sciences, including the formation of mantle plumes, the origin of anomalous geochemical signatures in the basalts they produce, and the rate at which convectively supported topography grows and decays. By taking a multi-pronged approach that integrates a full range of geodynamic, geodetic and seismological data with numerical models, we are able to place valuable new constraints on LLVP structure. Firstly, by using recent measurements of Earth's dynamic topography, CMB ellipticity, and geoid to determine optimal models of mantle flow, we find that—irrespective of assumed tomographic and rheologic configuration—anomalously dense material is concentrated within the basal $\sim$200 km of LLVPs. Secondly, we conclude that buoyancy variations associated with these seismically imaged features extend no more than ~ 900 km above the core-mantle boundary. Thirdly, we show that the apparent disagreement between LLVP buoyancy structures previously inferred from Stoneley mode and body tide inversions can be resolved using these optimised thermochemical models. Finally, by comparing an ensemble of thermodynamically self-consistent density models that cover a range of possible recycled and primordial compositions to a full suite of geodynamic, seismological, and geochemical constraints, we demonstrate that the dense basal material within the LLVPs likely comprises remnants of Hadean crust and chondritic regolith. These results confirm that basal sections of LLVPs are potential reservoirs for the primordial isotope signatures observed in oceanic island basalts. Our work further suggests that long-wavelength, convectively-driven topography evolves relatively slowly and is lower amplitude than would be expected if LLVPs were purely thermal features.

Appendix A Mantle density models

We develop two classes of mantle density models; the first based on inversion of geodynamic data, the second derived using thermodynamic forward modelling of proposed chemical compositions. To generate the first class of density models, we separate the mantle into six layers: 0–400 km (UUM = upper upper mantle), 400–670 km (LUM = lower upper mantle), 670–1000 km (UMM = upper mid-mantle), 1000–2000 km (LMM = lower mid-mantle), 2000–2700 km (ULM = upper lower mantle), and 2700–2891 km (LLM = lower lower mantle). Density in the UMM layer is determined from SLNAAFSA (Hoggard et al., 2020), which is a version of the SL2013sv (Schaeffer & Lebedev, 2013) upper mantle model into which the regional updates SL2013NA in North America (Schaeffer & Lebedev, 2014), AF2019 in Africa (Celli, Lebedev, Schaeffer, Ravenna, & Gaina, 2020), and SA2019 in South America and the South Atlantic Ocean (Celli, Lebedev, Schaeffer, & Gaina, 2020) have been incorporated. The baseline model, SL2013sv, has been shown to produce topographic predictions that are in good agreement with residual depth measurements, even at relatively short wavelengths (~ 1000 km; F. D. Richards et al., 2020).

Seismic velocities are converted into density within the UMM layer using an anelastic parameterisation following the methodology of F. D. Richards et al. (2020). This approach allows self-consistent mapping between seismic velocities and temperature, density, and viscosity variations, while correcting for discrepancies between tomographic models that result from parameterisation choices rather than true Earth structure. Optimal parameters determined for SLNAAFSA are: $\mu_0 = 75.9$ GPa; $\frac{\partial\mu}{\partial T} = -17.9$ MPa °C^{-1}; $\frac{\partial\mu}{\partial P} = 2.54$; $\eta_r = 10^{23.0}$ Pa s; $E_a = 489$ kJ mol^{-1}; $V_a = 0.63$ cm^3 mol^{-1}; and $\frac{\partial T_s}{\partial z} = 0.931$ °C km^{-1}. We assume that continental lithosphere, delineated by the $T = 1200$ °C isothermal surface, has neutral buoyancy and set density in these regions equal to the average density of all external material at the relevant depth in order to eliminate any direct dynamic topographic contribution. This assumption is based on heat flow measurements, xenolith geochemistry, seismic velocity, gravity, and topography observations that suggest compositional and thermal density contributions approximately balance each other within the continental lithosphere (Jordan, 1978; Shapiro et al., 1999).

Deeper than 300 km, seismic velocity perturbations from whole-mantle tomographic models LLNL-G3D-JPS (N. Simmons et al., 2015), S40RTS (Ritsema et al., 2011), SAVANI (Auer et al., 2014), SEMUCB-WM1 (French & Romanowicz, 2015), and TX2011 (Grand, 2002) are converted to density assuming constant $R_\rho = \partial\ln\rho/\partial\ln V_S$ values within each layer and that average density is equal to PREM (Dziewonski & Anderson, 1981). To ensure smooth transitions in density anomalies between the two input density parameterisations, we take their weighted average between 300 km and 400 km, beyond which the sensitivity of the surface wave-dominated upper mantle model tends to zero. Weighting coefficients of the respective tomographic models, w_{UM} and w_{WM}, vary linearly between 1 and 0 over this depth range and are combined according to $w_{UM} = 1 - w_{WM}$. R_ρ is fixed at 0.15 for the whole-mantle model between 300–400 km, based on the mean value within this layer inferred from SLNAAFSA.

The lower mantle layers, ULM and LLM, are laterally subdivided into regions outside (OULM and OLLM), and within the LLVPs (LULM and LLLM), each delineated using the -0.65% V_S anomaly contour of the whole-mantle tomographic model under investigation (Burke et al., 2008). Outside the LLVPs, R_ρ varies as $R_\rho = [0.1, 0.2, ...0.4]$ with the exception of the LMM layer (1000–2000 km), where a minimum bound on R_ρ of 0.0 is adopted allowing for limited mid-mantle seismic resolution and the potential presence of artefacts due to vertical smearing. Within the LLVPs, we apply a constant compositional density anomaly such that $\delta\rho(z) = R_\rho(i)\delta V_S(z) + \delta\rho_c(i)$, where $\delta\rho_c(i)$ is the intrinsic compositional density difference between LLVP material and ambient mantle (z is depth, i is the layer index, i.e., ULM or LLM). Note that, in contrast to studies that employ negative R_ρ values (Moulik & Ekström, 2016; Koelemeijer et al., 2017; Lau et al., 2017), this approach maximises intra-LLVP density around the edges of the low-velocity regions rather than within their central portions, and therefore assumes that, within each domain, internal V_S variations are controlled by temperature in the usual manner (Figure S7). This configuration is therefore consistent with the hypothesis that sharp compositional contrasts are responsible for strong lateral gradients in V_S across the LLVP boundaries (Ni et al., 2002). For our thermochemical models, $\delta\rho_c$ varies as $[0., 0.2, .., 2.0]$% within the LULM and LLLM regions, yielding a total of $\sim 2 \times 10^5$ input density structures. Note that, in the Supporting Information we also test the effect of: a) parameterising excess LLVP density using negative R_ρ values instead of an intrinsic density contrast and b) parameterising excess LLVP density using $\delta\rho_c$ values, but shifting the ULM-LLM boundary to 2800 km (see Text S1.2).

The second class of density models are created to investigate likely chemical compositions of the LLVPs. We generate a suite of density structures based on thermodynamic modelling of key candidate compositions and V_S variation from tomographic models (Table A1). For a given composition, Perple_X is used alongside the thermodynamic database of Stixrude & Lithgow-Bertelloni (2011) to generate a lookup table of anharmonic shear-wave velocities and densities by varying temperature as $[300, 350, ..4500]$ K and pressure as

Composition	SiO_2 (%)	MgO (%)	FeO (%)	CaO (%)	Al_2O_3 (%)	Na_2O (%)	Reference
Pyrolite	38.71	49.85	6.17	2.94	2.22	0.11	Workman & Hart, 2005
MORB	51.75	14.94	7.06	13.88	10.19	2.18	Workman & Hart, 2005
CEB	48.47	20.00	11.28	10.59	8.16	1.50	Tolstikhin & Hofmann, 2005
FSP	40.15	41.98	12.90	2.82	1.92	0.23	Lee et al., 2010

Table A1. Molar oxide ratios for different mantle compositional endmembers. MORB = present-day mid-ocean ridge basalt; CEB = chondrite-enriched basalt; FSP = iron-enriched pyrolite.

$[0., 0.1, ...140]$ GPa (Text S2.1). At each depth, temperature-dependent discontinuities in density and seismic velocity caused by phase transitions are smoothed by adopting the median temperature derivative across a $\pm 500^\circ$C swath either side of the geotherm. Smoothed anharmonic velocities are then corrected for anelasticity using a Q profile determined using the approach of Matas & Bukowinski (2007), as outlined in Lu et al. (2020) (Text S2.2; Figure S11). Having smoothed and corrected the V_S lookup table, velocities from a given seismic tomographic model can be converted into temperature at each depth, with values adjusted by a constant offset to ensure mean temperatures are consistent with the mantle geotherm. These temperatures are then used to extract the corresponding buoyancy structure from the smoothed density lookup table. In cases where compositions are not equivalent to a particular endmember, properties appropriate for a mechanical mixture of the two components are calculated using the Voigt-Reuss-Hill approximation to average the elastic moduli. When the composition of the LLVP is distinct from ambient mantle, temperatures and densities are determined separately for the two components and then combined into a single array, with the boundary corresponding to the -0.65% V_S anomaly contour (Burke et al., 2008). All models assume that the range of possible mantle compositions is some combination of pyrolite and a specific dense component; either mid-ocean ridge basalt (Workman & Hart, 2005), chondrite-enriched basalt (Tolstikhin & Hofmann, 2005), or iron-enriched pyrolite (Lee et al., 2010). For each component, we generate models for compositional enrichments of $[0, 10, ..., 100]$% and for upper boundaries of the dense layer between 2000 km and 2800 km in 100 km increments, as well as testing 2850 km.

In the upper 300 km of the mantle, density structure is identical to the first class of models. Below 400 km, densities are taken directly from the thermodynamically self-consistent parameterisation described above, whilst between 300 km and 400 km depth, densities derived from the two parameterisations are smoothly merged by taking their weighted average, as described for the first class of models. Since optimal thermal and thermochemical density models recovered from geodynamic inversions consistently find that R_ρ(LMM) ~ 0, density anomalies in the 1000–2000 km depth interval are set to zero for all models, although by using a high-pass filter to remove degree-two structure, we also test the effect of including only small-scale density anomalies in this depth region, described further in the Supporting Information (Text S1.3; Figure S14).

Appendix B Mantle flow simulations

Using the suite of thermal and thermochemical mantle density models, we predict surface and CMB dynamic topography and geoid undulations for $1 \leq l \leq 30$ using an instantaneous flow kernel methodology. As Earth's viscosity structure is uncertain, we assess the sensitivity of our mantle flow results to three different radial profiles that are constrained by geoid, heat flow and glacial isostatic adjustment observations: `S10` (Steinberger et al., 2010); `F10V1` (Forte et al., 2010); and `F10V2` (Forte et al., 2010).

To calculate instantaneous mantle flow, we exploit the sensitivity kernel methodology originally implemented by Hager & O'Connell (1979) and M. A. Richards & Hager (1984), extended by Corrieu et al. (1995) to account for the effects of compressibility and self-gravitation. This approach applies the propagator matrix technique to solve the equations governing conservation of mass and momentum within a highly viscous spherical shell, alongside Poisson's equation for gravity, to generate kernels describing the linear relationship between geodynamic observables (dynamic topography, geoid and CMB topography) and laterally varying density anomalies across the mantle. We impose free-slip surface and CMB boundary conditions. For each assumed viscosity profile, the resulting sensitivity kernels vary as a function of depth and the spherical harmonic degree under consideration. Dynamic topography δA^{lm} can then be determined using

$$\delta A^{lm} = \frac{1}{\Delta\rho_0} \int_{R_C}^{R_\oplus} K_A^l(r) \delta\rho^{lm}(r) dr \tag{B1}$$

where K_A^l is the dynamic topography kernel, r is radius, $\Delta\rho_0$ is the density difference between the uppermost mantle ($\rho_0 = 3380$ kg m^{-3}; Dziewonski & Anderson, 1981) and water ($\rho_w = 1030$ kg m^{-3}), l and m are spherical harmonic degree and order, $R_\oplus = 6371$ km and $R_C = 3480$ km are the radii of the Earth and CMB, respectively, and $\delta\rho^{lm}(r)$ represents the driving density anomalies in the spherical harmonic expansion. The geoid, δN^{lm}, is calculated using

$$\delta N^{lm} = \frac{4\pi\gamma R_\oplus}{(2l+1)\, g_{R_\oplus}} \int_{R_C}^{R_\oplus} K_N^l(r) \delta\rho^{lm}(r) dr \tag{B2}$$

where K_N^l is the geoid kernel, $g_{R_\oplus}$ is surface gravity and γ is the gravitational constant. CMB topography, δC^{lm}, is determined according to

$$\delta C^{lm} = -\frac{1}{\Delta\rho_C} \int_{R_C}^{R_\oplus} K_C^l(r) \delta\rho^{lm}(r) dr \tag{B3}$$

where K_C^l is the CMB topography kernel and $\Delta\rho_C$ is the density difference between the lowermost mantle ($\rho_C = 5570$ kg m^{-3}) and the uppermost outer core ($\rho_{OC} = 9900$ kg m^{-3}; Dziewonski & Anderson, 1981).

Applying this kernel formalism permits rapid calculation of key observables, enabling the more complete exploration of parameter space that is central to this study. This method, however, cannot incorporate lateral viscosity variations (LVVs). While LVVs are undoubtedly present within the Earth, numerous studies conclude that they generate minimal differences in the geodynamical observations we explore here compared with those resulting from variability in density inputs derived from different tomographic models (Moucha et al., 2007; Ghosh et al., 2010; Yang & Gurnis, 2016). We therefore anticipate that our main conclusions remain valid for reasonable amplitudes of LVV.

Appendix C Misfit to geodynamic observations

We assess model performance using a combined misfit function to assess compatibility with geoid, dynamic topography and excess CMB ellipticity constraints. Following previous studies (Steinberger & Calderwood, 2006; N. A. Simmons et al., 2009), we define the misfit to geoid and dynamic topography based on variance reduction (VR), a proxy for the proportion of observed signal explained by a given model prediction. Geoid misfit, χ_N, is defined to be equivalent to $1 - \mathrm{VR}_N$, where VR_N represents geoid variance reduction, and is calculated globally using

$$\chi_N = \frac{\sum_{l=2}^{l_{max}} \sum_{m=-l}^{l} \left(N_c^{lm} - N_o^{lm}\right)^2}{\sum_{l=2}^{l_{max}} \sum_{m=-l}^{l} \left(N_o^{lm}\right)^2} \tag{C1}$$

where N^{lm} terms represent spherical harmonic coefficients of observed (subscript o) and predicted (subscript c) geoid, and $l_{max} = 30$ is the maximum spherical harmonic degree.

Dynamic topography misfit, χ_A, is defined analogously to χ_N (i.e., $\chi_A = 1-\mathrm{VR}_A$). However, since accurate residual depth measurements only exist at specific oceanic locations, rather than compare spherical harmonic coefficients, we instead determine this value in the spatial domain according to

$$\chi_A = \frac{\sum_{n_A=1}^{N_A}\left[\left(A_c^i - A_o^i\right) - \overline{\left(A_c^i - A_o^i\right)}\right]^2}{\sum_{n_A=1}^{N_A}\left(A_o^i - \overline{A_o^i}\right)^2} \tag{C2}$$

where A^i terms are predicted and observed dynamic topography at $N_A = 2278$ geographic locations (Hoggard et al., 2017), and values are weighted by the surface area of the 1° bin associated with each data point in order to correct for latitudinal variation in sampling density. Since excess CMB ellipticity is defined using a single spherical harmonic coefficient, rather than using a variance reduction-based misfit definition, we use the expression

$$\chi_C = \sqrt{\left(\frac{C_c^{20} - C_o^{20}}{\sigma_{C_o^{20}}}\right)^2} \tag{C3}$$

for this component, which is similar to previous studies (Steinberger & Holme, 2008; N. A. Simmons et al., 2009). C^{20} terms represent the $l = 2$, $m = 0$ coefficient of observed and modelled core-mantle boundary topography, and $\sigma_{C_o^{20}} = 100$ m based on the range of reported values (Gwinn et al., 1986; Mathews et al., 2002; Dehant et al., 2017). Finally, we sum each of these three components into a combined geodynamic misfit function,

$$\chi_G = \chi_N + \chi_A + \chi_C \tag{C4}$$

In Figure 2, we present optimal results for the S10 viscosity profile (Steinberger et al., 2010) and TX2011 tomographic model (Grand, 2002), whilst Figures S1–S6 display results for other combinations. We select this tomographic model as it generates geodynamic predictions with the lowest overall misfit. We choose the S10 (Steinberger et al., 2010) viscosity profile over F10V1 (Forte et al., 2010)—despite the latter yielding lower misfits—since it does not include a very low viscosity (7×10^{19} Pa s) layer at the base of the transition zone, which is considered to be controversial since it requires the entire region to be nearly water-saturated ($\sim 1.5\%$; Fei et al., 2017). Nevertheless, we acknowledge that a recent joint analysis of geodynamic and seismic tomographic models is consistent with the presence of a low-viscosity layer at 660 km depth (Rudolph et al., 2021).

Appendix D Body tide and Stoneley mode predictions

Modelling of Earth's body tidal response requires models of 3D elastic, 3D density, and 1D anelastic structure (Lau et al., 2017). In the upper 400 km of the mantle, 3D elastic structure is determined using the calibrated parameterisation of SLNAAFSA to remove anelastic reductions in V_S from the seismic tomographic model, leaving only anharmonic V_S variations (V_S^{anh}). Below 300 km, V_S^{anh} is derived from the tomographic values, V_S^{anel}, using radial changes in shear attenuation, Q_S^{-1}, from PREM and the expression

$$V_S^{anel} = V_S^{anh}\left[1 - \frac{Q_S^{-1}}{2\tan(\pi\alpha/2)}\right] \tag{D1}$$

where $\alpha = 0.15$ (Dziewonski & Anderson, 1981; Karato, 1993; Widmer et al., 1992). While the resulting 3D V_S^{anh} model constrains the unrelaxed shear modulus, unrelaxed bulk modulus variations are obtained from V_ϕ^{anh}, assuming that

$$R_b = \frac{\partial \ln V_\phi}{\partial \ln V_S} \approx \frac{\partial \ln V_\phi^{anh}}{\partial \ln V_S^{anh}} = 0.05 \tag{D2}$$

and the radial V_ϕ^{anh} profile can be determined using the same V_S–V_ϕ scaling as PREM (Dziewonski & Anderson, 1981). The 1D anelastic structure applied to determine elastic modulus dispersion at the 12-hour period of the M2 body tide adopts the mean value of Q_S^{-1} obtained from the calibrated parameterisation of SLNAAFSA at depths above 400 km, and that of PREM at greater depths.

With the Earth model specified, the body tide response is computed using full-coupling normal mode perturbation theory, with shear and bulk moduli dispersion calculated at tidal frequencies using IERS standards (Widmer et al., 1992; Lau et al., 2015). Following Lau et al. (2017), the fit between the predicted and observed in-phase M2 body tide displacement is assessed at the sites of GPS stations by determining whether inclusion of 3D elastic and density structure significantly enhances coherence between the two fields compared with a baseline 1D model (PREM; Dziewonski & Anderson, 1981). The 3D Earth model is only considered to yield a statistically significant improvement if the correlation obtained between 'raw' and 'corrected' GPS residuals exceeds that obtained for the 1D model at the 95% significance level, accounting for correlation between GPS estimates due to the uneven spatial distribution of receivers. Raw residuals represent observed M2 body tide displacements minus those predicted for the 1D model. Corrected residuals also account for the effects of Moho and CMB excess ellipticity, Earth rotation and ocean tidal loading, and, in the 3D model case, incorporate an additional correction for differences in the body tide displacement predicted using 3D versus 1D structure.

To predict Stoneley mode splitting functions, 3D variations in V_S, V_P and CMB topography must be specified in addition to the density model (Resovsky & Ritzwoller, 1998). V_S anomalies are drawn directly from the tomographic model used to construct a given density model, while V_P is determined by scaling V_S anomalies using a constant value of $R_P = \partial \mathrm{ln} V_P / \partial \mathrm{ln} V_S = 0.5$ (Ritsema et al., 2004). We do not consider seismic anisotropy. CMB topography is determined self-consistently using instantaneous flow simulations for each density and viscosity model combination.

For a specified input velocity, density and topography model, Stoneley mode splitting coefficients, $\mathcal{C}^{st}$ can be calculated using the expression

$$\mathcal{C}^{st} = \int_{R_C}^{R_\oplus} \mathrm{dln}\mathbf{M}^{st}(r) \cdot \mathbf{K}_M^s(r) r^2 \mathrm{d}r + \mathrm{dln}C^{st} K_C^s \tag{D3}$$

where $\mathrm{dln}\mathbf{M}^{st}(r)$ represents the prescribed 3D V_S, V_P, and density heterogeneity at angular degree, s, order, t, and radius, r. $\mathbf{K}_M^s(r)$ are the relevant sensitivity kernels calculated using PREM (Woodhouse, 1980; Dziewonski & Anderson, 1981), $\mathrm{dln}C^{st}$ is the CMB topography (the discontinuity most important for Stoneley modes), and K_C^s is the associated sensitivity kernel.

The misfit between predicted and observed Stoneley mode splitting functions, χ_S is

$$\chi_S = \frac{1}{N_S} \sum_{n_S=1}^{N_S} \frac{\sum_{s=2}^{s_{max}} \sum_{t=-s}^{s} (\mathcal{C}_c^{st} - \mathcal{C}_o^{st})^2}{\sum_{s=2}^{s_{max}} \sum_{t=-s}^{s} (\mathcal{C}_o^{st})^2} \tag{D4}$$

where $N_S = 9$ is the number of individual Stoneley modes investigated, the second summation term includes only even degree terms, where s_{max} is the maximum order. In most calculations $s_{max} = 2$; however, we also test the impact of setting s_{max} to the maximum degree at which splitting function measurements are available for a particular mode, as well as the consequences of adopting different misfit criteria (Text S1.4; Table S4) and ignoring CMB topography (Text S2.3; Figure S12).

We combine χ_S and χ_G to yield a joint total misfit function, χ_T, using

$$\chi_T = w_G \chi_G + w_S \chi_S \tag{D5}$$

where $w_G = 0.5$ and $w_S = 5$. These weightings result in misfit values with comparable global minima.

Acknowledgments

F.D.R. acknowledges support from the Imperial College Research Fellowship Scheme and the Schmidt Science Fellows program, in partnership with the Rhodes Trust. M.J.H. acknowledges support from the National Aeronautics and Space Administration (grant NNX17AE17G), the Donors of the American Chemical Society Petroleum Research Fund (59062-DNI8), and Geoscience Australia. M.J.H. and S.G. are supported by the G-ADOPT project, which is funded by the Australian Research Data Commons (https://doi.org/10.47486/PL031). P.K. acknowledges support from a Royal Society University Research Fellowship (URF\R1\180377). H.C.P.L. acknowledges support from NSF (EAR-192386). We thank D. Al-Attar, J. Austermann, L. Colli, D. R. Davies, R. Hawkins, M. Sambridge, Y. Takei, A. Valentine, N. White and J. Winterbourne for their help. Figures were prepared using Generic Mapping Tools software.

References

Arevalo Jr, R., McDonough, W. F., Stracke, A., Willbold, M., Ireland, T. J., & Walker, R. J. (2013). Simplified mantle architecture and distribution of radiogenic power. *Geochemistry, Geophysics, Geosystems*, *14*(7), 2265–2285.

Auer, L., Boschi, L., Becker, T., Nissen-Meyer, T., & Giardini, D. (2014). Savani: A variable resolution whole-mantle model of anisotropic shear velocity variations based on multiple data sets. *Journal of Geophysical Research: Solid Earth*, *119*(4), 3006–3034.

Burke, K., Steinberger, B., Torsvik, T. H., & Smethurst, M. A. (2008). Plume generation zones at the margins of large low shear velocity provinces on the core–mantle boundary. *Earth and Planetary Science Letters*, *265*(1-2), 49–60.

Castillo, P. (1988). The dupal anomaly as a trace of the upwelling lower mantle. *Nature*, *336*(6200), 667–670.

Celli, N. L., Lebedev, S., Schaeffer, A. J., & Gaina, C. (2020). African cratonic lithosphere carved by mantle plumes. *Nature Communications*, *11*(92), 1–10. doi: 10.1038/s41467-019-13871-2

Celli, N. L., Lebedev, S., Schaeffer, A. J., Ravenna, M., & Gaina, C. (2020). The upper mantle beneath the South Atlantic Ocean, South America and Africa from waveform tomography with massive data sets. *Geophysical Journal International*, *221*, 178–204. doi: 10.1093/gji/ggz574

Chambat, F., Ricard, Y., & Valette, B. (2010). Flattening of the Earth: further from hydrostaticity than previously estimated. *Geophysical Journal International*, *183*(2), 727–732.

Connolly, J. A. D. (2005, jul). Computation of phase equilibria by linear programming: A tool for geodynamic modeling and its application to subduction zone decarbonation. *Earth and Planetary Science Letters*, *236*(1-2), 524–541. doi: 10.1016/J.EPSL.2005.04.033

Connolly, J. A. D., & Khan, A. (2016). Uncertainty of mantle geophysical properties computed from phase equilibrium models. *Geophys. Res. Lett.*, *43*(10), 5026-5034. doi: 10.1002/2016GL068239

Corrieu, V., Thoraval, C., & Ricard, Y. (1995). Mantle dynamics and geoid Green functions. *Geophysical Journal International*, *120*(2), 516–523.

Cottaar, S., & Lekic, V. (2016). Morphology of seismically slow lower-mantle structures. *Geophysical Journal International*, *207*(2), 1122-1136. doi: 10.1093/gji/ggw324

Davaille, A., & Romanowicz, B. (2020). Deflating the LLSVPs: Bundles of Mantle Thermochemical Plumes Rather Than Thick Stagnant "Piles". *Tectonics*, *39*(10), e2020TC006265.

Davies, D. R., Goes, S., Davies, J. H., Schuberth, B., Bunge, H.-P., & Ritsema, J. (2012). Reconciling dynamic and seismic models of Earth's lower mantle: The dominant role of thermal heterogeneity. *Earth and Planetary Science Letters*, *353*, 253–269.

Davies, D. R., Valentine, A., Kramer, S., Rawlinson, N., Hoggard, M., Eakin, C., & Wilson, C. (2019). Earth's multi-scale topographic response to global mantle flow. *Nature*

Geoscience, *12*(10), 845–850.
Day, J. M., Jones, T. D., & Nicklas, R. W. (2022). Mantle sources of ocean islands basalts revealed from noble gas isotope systematics. *Chemical Geology*, *587*, 120626.
Dehant, V., Laguerre, R., Rekier, J., Rivoldini, A., Triana, S. A., Trinh, A., ... Zhu, P. (2017). Understanding the effects of the core on the nutation of the Earth. *Geodesy and Geodynamics*, *8*(6), 389–395.
Della Mora, S., Boschi, L., Tackley, P., Nakagawa, T., & Giardini, D. (2011). Low seismic resolution cannot explain s/p decorrelation in the lower mantle. *Geophysical Research Letters*, *38*(12).
Deschamps, F., Cobden, L., & Tackley, P. J. (2012). The primitive nature of large low shear-wave velocity provinces. *Earth and Planetary Science Letters*, *349*, 198–208.
Deschamps, F., & Tackley, P. J. (2009). Searching for models of thermo-chemical convection that explain probabilistic tomography. ii—influence of physical and compositional parameters. *Physics of the Earth and Planetary Interiors*, *176*(1-2), 1–18.
Dupré, B., & Allègre, C. J. (1983). Pb–sr isotope variation in indian ocean basalts and mixing phenomena. *Nature*, *303*(5913), 142–146.
Dziewonski, A. M., & Anderson, D. L. (1981). Preliminary reference Earth model. *Physics of the Earth and Planetary Interiors*, *25*(4), 297–356.
Fei, H., Yamazaki, D., Sakurai, M., Miyajima, N., Ohfuji, H., Katsura, T., & Yamamoto, T. (2017). A nearly water-saturated mantle transition zone inferred from mineral viscosity. *Science Advances*, *3*(6), e1603024.
Förste, C., Flechtner, F., Schmidt, R., Stubenvoll, R., Rothacher, M., Kusche, J., ... others (2008). Eigen-gl05c-a new global combined high-resolution grace-based gravity field model of the gfz-grgs cooperation. In *General assembly european geosciences union (vienna, austria 2008).*
Forte, A. M., & Mitrovica, J. X. (2001). Deep-mantle high-viscosity flow and thermochemical structure inferred from seismic and geodynamic data. *Nature*, *410*(6832), 1049–1056.
Forte, A. M., Quéré, S., Moucha, R., Simmons, N. A., Grand, S. P., Mitrovica, J. X., & Rowley, D. B. (2010). Joint seismic–geodynamic-mineral physical modelling of African geodynamics: A reconciliation of deep-mantle convection with surface geophysical constraints. *Earth and Planetary Science Letters*, *295*(3-4), 329–341.
French, S. W., & Romanowicz, B. (2015). Broad plumes rooted at the base of the Earth's mantle beneath major hotspots. *Nature*, *525*(7567), 95–99. doi: 10.1038/nature14876
Garnero, E. J., McNamara, A. K., & Shim, S.-H. (2016). Continent-sized anomalous zones with low seismic velocity at the base of Earth's mantle. *Nature Geoscience*, *9*(7), 481–489.
Ghelichkhan, S., & Bunge, H.-P. (2018). The adjoint equations for thermochemical compressible mantle convection: derivation and verification by twin experiments. *Proceedings of the Royal Society A*, *474*(2220), 20180329.
Ghosh, A., Becker, T., & Zhong, S. (2010). Effects of lateral viscosity variations on the geoid. *Geophysical Research Letters*, *37*(1), L01301.
Gleeson, M., Soderman, C., Matthews, S., Cottaar, S., & Gibson, S. (2021). Geochemical constraints on the structure of the earth's deep mantle and the origin of the llsvps. *Geochemistry, Geophysics, Geosystems*, *22*(9), e2021GC009932.
Grand, S. P. (2002). Mantle shear–wave tomography and the fate of subducted slabs. *Philosophical Transactions of the Royal Society of London. Series A: Mathematical, Physical and Engineering Sciences*, *360*(1800), 2475–2491.
Gurnis, M., Mitrovica, J. X., Ritsema, J., & van Heijst, H.-J. (2000). Constraining mantle density structure using geological evidence of surface uplift rates: The case of the African Superplume. *Geochem., Geophys., Geosyst.*, *1*(7), 1999GC000035. doi: 10.1029/1999GC000035
Gwinn, C. R., Herring, T. A., & Shapiro, I. I. (1986). Geodesy by radio interferometry: Studies of the forced nutations of the Earth: 2. Interpretation. *Journal of Geophysical Research: Solid Earth*, *91*(B5), 4755–4765.
Hager, B. H., Clayton, R. W., Richards, M. A., Comer, R. P., & Dziewonski, A. M. (1985).

Lower mantle heterogeneity, dynamic topography and the geoid. *Nature*, *313*(6003), 541–545. doi: 10.1038/313541a0

Hager, B. H., & O'Connell, R. J. (1979). Kinematic models of large-scale flow in the Earth's mantle. *Journal of Geophysical Research*, *84*(B3), 1031–1048. doi: 10.1029/JB084iB03p01031

Hart, S. R. (1984). A large-scale isotope anomaly in the southern hemisphere mantle. *Nature*, *309*(5971), 753–757.

Hernlund, J. W., & Houser, C. (2008). On the statistical distribution of seismic velocities in earth's deep mantle. *Earth and Planetary Science Letters*, *265*(3-4), 423–437.

Herzberg, C. (2016). Petrological evidence from komatiites for an early earth carbon and water cycle. *Journal of Petrology*, *57*(11-12), 2271–2288.

Hoggard, M. J., Czarnota, K., Richards, F. D., Huston, D. L., Jaques, A. L., & Ghelichkhan, S. (2020). Global distribution of sediment-hosted metals controlled by craton edge stability. *Nature Geoscience*, *13*, 504–510.

Hoggard, M. J., White, N., & Al-Attar, D. (2016). Global dynamic topography observations reveal limited influence of large-scale mantle flow. *Nature Geoscience*, *9*, 456—463.

Hoggard, M. J., Winterbourne, J., Czarnota, K., & White, N. (2017). Oceanic residual depth measurements, the plate cooling model, and global dynamic topography. *Journal of Geophysical Research: Solid Earth*, *122*(3), 2328–2372.

Ishii, M., & Tromp, J. (2001). Even-degree lateral variations in the Earth's mantle constrained by free oscillations and the free-air gravity anomaly. *Geophysical Journal International*, *145*(1), 77–96.

Jones, T. D., Davies, D. R., & Sossi, P. (2019). Tungsten isotopes in mantle plumes: Heads it's positive, tails it's negative. *Earth and Planetary Science Letters*, *506*, 255–267.

Jones, T. D., Maguire, R. R., van Keken, P. E., Ritsema, J., & Koelemeijer, P. (2020). Subducted oceanic crust as the origin of seismically slow lower-mantle structures. *Progress in Earth and Planetary Science*, *7*, 1–16.

Jordan, T. H. (1978). Composition and development of the continental tectosphere. *Nature*, *274*(5671), 544–548.

Karato, S.-I. (1993). Importance of anelasticity in the interpretation of seismic tomography. *Geophysical Research Letters*, *20*(15), 1623–1626.

Karato, S.-I., & Karki, B. B. (2001). Correction to" origin of lateral variation of seismic wave velocities and density in the deep mantle. *Journal of Geophysical Research*, *106*(B12), 30–623.

Kellogg, L. H., Hager, B. H., & van der Hilst, R. D. (1999). Compositional stratification in the deep mantle. *Science*, *283*(5409), 1881–1884.

Koelemeijer, P. (2021). Towards consistent seismological models of the core-mantle boundary landscape. In H. Marquardt, M. Ballmer, S. Cottaar, & J. G. Konter (Eds.), *Mantle Convection and Surface Expressions* (Vol. 1, p. 512). Wiley Online Library. doi: doi:10.1002/9781119528609.ch9

Koelemeijer, P., Deuss, A., & Ritsema, J. (2017). Density structure of Earth's lowermost mantle from Stoneley mode splitting observations. *Nature Communications*, *8*(1), 1–10.

Koelemeijer, P., Schuberth, B., Davies, D., Deuss, A., & Ritsema, J. (2018). Constraints on the presence of post-perovskite in Earth's lowermost mantle from tomographic-geodynamic model comparisons. *Earth and Planetary Science Letters*, *494*, 226–238. doi: https://doi.org/10.1016/j.epsl.2018.04.056

Labrosse, S., Hernlund, J., & Coltice, N. (2007). A crystallizing dense magma ocean at the base of the Earth's mantle. *Nature*, *450*(7171), 866–869.

Lau, H. C., Mitrovica, J. X., Davis, J. L., Tromp, J., Yang, H.-Y., & Al-Attar, D. (2017). Tidal tomography constrains Earth's deep-mantle buoyancy. *Nature*, *551*(7680), 321–326.

Lau, H. C., Yang, H.-Y., Tromp, J., Mitrovica, J. X., Latychev, K., & Al-Attar, D. (2015). A normal mode treatment of semi-diurnal body tides on an aspherical, rotating and anelastic Earth. *Geophysical Journal International*, *202*(2), 1392–1406.

Lee, C.-T. A., Luffi, P., Höink, T., Li, J., Dasgupta, R., & Hernlund, J. (2010). Upside-down differentiation and generation of a 'primordial' lower mantle. *Nature*, *463*(7283), 930–933.

Li, M., & McNamara, A. K. (2013). The difficulty for subducted oceanic crust to accumulate at the earth's core-mantle boundary. *Journal of Geophysical Research: Solid Earth*, *118*(4), 1807–1816.

Li, M., & McNamara, A. K. (2018). The influence of deep mantle compositional heterogeneity on earth's thermal evolution. *Earth and Planetary Science Letters*, *500*, 86–96.

Li, M., McNamara, A. K., & Garnero, E. J. (2014). Chemical complexity of hotspots caused by cycling oceanic crust through mantle reservoirs. *Nature Geoscience*, *7*(5), 366–370.

Li, Y., Deschamps, F., & Tackley, P. J. (2014). The stability and structure of primordial reservoirs in the lower mantle: insights from models of thermochemical convection in three-dimensional spherical geometry. *Geophysical Journal International*, *199*(2), 914–930.

Liu, X., & Zhong, S. (2016). Constraining mantle viscosity structure for a thermochemical mantle using the geoid observation. *Geochemistry, Geophysics, Geosystems*, *17*(3), 895–913.

Lu, C., Forte, A. M., Simmons, N. A., Grand, S. P., Kajan, M. N., Lai, H., & Garnero, E. J. (2020). The Sensitivity of Joint Inversions of Seismic and Geodynamic Data to Mantle Viscosity. *Geochemistry, Geophysics, Geosystems*, *21*(4), e2019GC008648.

Maguire, R., Ritsema, J., Bonnin, M., van Keken, P. E., & Goes, S. (2018). Evaluating the resolution of deep mantle plumes in teleseismic traveltime tomography. *Journal of Geophysical Research: Solid Earth*, *123*(1), 384–400.

Matas, J., & Bukowinski, M. S. (2007). On the anelastic contribution to the temperature dependence of lower mantle seismic velocities. *Earth and Planetary Science Letters*, *259*(1-2), 51–65.

Mathews, P. M., Herring, T. A., & Buffett, B. A. (2002). Modeling of nutation and precession: New nutation series for nonrigid Earth and insights into the Earth's interior. *Journal of Geophysical Research: Solid Earth*, *107*(B4), ETG–3.

McKay, D. S., Heiken, G., Basu, A., Blanford, G., Simon, S., Reedy, R., ... Papike, J. (1991). The lunar regolith. *Lunar Sourcebook: A User's Guide to the Moon*, *567*, 285–356.

McNamara, A. K., & Zhong, S. (2004). Thermochemical structures within a spherical mantle: Superplumes or piles? *Journal of Geophysical Research: Solid Earth*, *109*(B7), B07402.

Moucha, R., Forte, A., Mitrovica, J., & Daradich, A. (2007). Lateral variations in mantle rheology: implications for convection related surface observables and inferred viscosity models. *Geophysical Journal International*, *169*(1), 113–135.

Moulik, P., & Ekström, G. (2016). The relationships between large-scale variations in shear velocity, density, and compressional velocity in the Earth's mantle. *Journal of Geophysical Research: Solid Earth*, *121*(4), 2737–2771.

Mulyukova, E., Steinberger, B., Dabrowski, M., & Sobolev, S. V. (2015). Survival of LLSVPs for billions of years in a vigorously convecting mantle: Replenishment and destruction of chemical anomaly. *Journal of Geophysical Research: Solid Earth*, *120*(5), 3824–3847.

Mundl-Petermeier, A., Walker, R., Fischer, R., Lekic, V., Jackson, M., & Kurz, M. (2020). Anomalous 182w in high 3he/4he ocean island basalts: Fingerprints of earth's core? *Geochimica et Cosmochimica Acta*, *271*, 194–211.

Ni, S., Tan, E., Gurnis, M., & Helmberger, D. (2002). Sharp sides to the African superplume. *Science*, *296*(5574), 1850–1852.

Niu, Y. (2018). Origin of the LLSVPs at the base of the mantle is a consequence of plate tectonics – A petrological and geochemical perspective. *Geoscience Frontiers*, *9*(5), 1265–1278. doi: https://doi.org/10.1016/j.gsf.2018.03.005

Resovsky, J. S., & Ritzwoller, M. H. (1998). New and refined constraints on three-dimensional Earth structure from normal modes below 3 mHz. *Journal of Geophysical*

Research: Solid Earth, *103*(B1), 783–810.

Ricard, Y., Richards, M., Lithgow-Bertelloni, C., & Lestunff, Y. (1993). A Geodynamic Model of Mantle Density Heterogeneity. *Journal of Geophysical Research: Solid Earth*, *98*(B12), 21895–21909. doi: 10.1029/93JB02216

Richards, F. D., Hoggard, M. J., White, N., & Ghelichkhan, S. (2020). Quantifying the relationship between short-wavelength dynamic topography and thermomechanical structure of the upper mantle using calibrated parameterization of anelasticity. *Journal of Geophysical Research: Solid Earth*, *125*(9), e2019JB019062.

Richards, M. A., & Hager, B. H. (1984). Geoid anomalies in a dynamic Earth. *Journal of Geophysical Research: Solid Earth*, *89*(B7), 5987–6002. doi: 10.1029/JB089iB07p05987

Ritsema, J., Deuss, A., Van Heijst, H. J., & Woodhouse, J. H. (2011). S40RTS: A degree-40 shear-velocity model for the mantle from new Rayleigh wave dispersion, teleseismic traveltime and normal-mode splitting function measurements. *Geophysical Journal International*, *184*, 1223–1236. doi: 10.1111/j.1365-246X.2010.04884.x

Ritsema, J., McNamara, A. K., & Bull, A. L. (2007). Tomographic filtering of geodynamic models: Implications for model interpretation and large-scale mantle structure. *Journal of Geophysical Research: Solid Earth*, *112*(B1).

Ritsema, J., van Heijst, H. J., & Woodhouse, J. H. (2004). Global transition zone tomography. *Journal of Geophysical Research: Solid Earth*, *109*(B2), B02302. doi: 10.1029/2003JB002610

Robson, A., Lau, H. C. P., Koelemeijer, P., & Romanowicz, B. (2022). An analysis of core–mantle boundary stoneley mode sensitivity and sources of uncertainty. *Geophysical Journal International*, *228*(3), 1962–1974.

Rudolph, M. L., Lourenço, D. L., Moulik, P., & Lekić, V. (2021). Long-wavelength mantle structure: Geophysical constraints and dynamical models. *Mantle Convection and Surface Expressions*, 1–19.

Schaeffer, A. J., & Lebedev, S. (2013). Global shear speed structure of the upper mantle and transition zone. *Geophysical Journal International*, *194*(1), 417–449. doi: 10.1093/gji/ggt095

Schaeffer, A. J., & Lebedev, S. (2014). Imaging the North American continent using waveform inversion of global and USArray data. *Earth and Planetary Science Letters*, *402*, 26–41. doi: 10.1016/j.epsl.2014.05.014

Schuberth, B. S. A., Bunge, H. P., Steinle-Neumann, G., Moder, C., & Oeser, J. (2009). Thermal versus elastic heterogeneity in high-resolution mantle circulation models with pyrolite composition: High plume excess temperatures in the lowermost mantle. *Geochem. Geophys. Geosyst.*, *10*(1), Q01W01. doi: 10.1029/2008GC002235

Shapiro, S. S., Hager, B. H., & Jordan, T. H. (1999). The continental tectosphere and Earth's long-wavelength gravity field. *Lithos*, *48*(1-4), 135–152.

Simmons, N., Myers, S., Johannesson, G., Matzel, E., & Grand, S. (2015). Evidence for long-lived subduction of an ancient tectonic plate beneath the southern Indian Ocean. *Geophysical Research Letters*, *42*(21), 9270–9278.

Simmons, N. A., Forte, A. M., & Grand, S. P. (2009). Joint seismic, geodynamic and mineral physical constraints on three-dimensional mantle heterogeneity: Implications for the relative importance of thermal versus compositional heterogeneity. *Geophysical Journal International*, *177*(3), 1284–1304.

Steinberger, B., & Calderwood, A. R. (2006). Models of large-scale viscous flow in the Earth's mantle with constraints from mineral physics and surface observations. *Geophysical Journal International*, *167*(3), 1461–1481. doi: 10.1111/j.1365-246X.2006.03131.x

Steinberger, B., Conrad, C. P., Tutu, A. O., & Hoggard, M. J. (2019). On the amplitude of dynamic topography at spherical harmonic degree two. *Tectonophysics*, *760*, 221–228.

Steinberger, B., & Holme, R. (2008). Mantle flow models with core-mantle boundary constraints and chemical heterogeneities in the lowermost mantle. *Journal of Geophysical Research: Solid Earth*, *113*(B5), B05403.

Steinberger, B., Werner, S. C., & Torsvik, T. H. (2010). Deep versus shallow origin of gravity anomalies, topography and volcanism on Earth, Venus and Mars. *Icarus*, *207*(2), 564–577.

Stixrude, L., & Lithgow-Bertelloni, C. (2011). Thermodynamics of mantle minerals–II. Phase equilibria. *Geophysical Journal International*, *184*(3), 1180–1213. doi: 10.1111/j.1365-246X.2010.04890.x

Stixrude, L., & Lithgow-Bertelloni, C. (2012). Geophysics of chemical heterogeneity in the mantle. *Annual Review of Earth and Planetary Sciences*, *40*, 569–595.

Su, W.-J., & Dziewonski, A. M. (1997). Simultaneous inversion for 3-D variations in shear and bulk velocity in the mantle. *Physics of the Earth and Planetary Interiors*, *100*(1-4), 135–156.

Sun, D., & Miller, M. S. (2013). Study of the western edge of the african large low shear velocity province. *Geochemistry, Geophysics, Geosystems*, *14*(8), 3109–3125.

Tackley, P. J. (2012). Dynamics and evolution of the deep mantle resulting from thermal, chemical, phase and melting effects. *Earth-Science Reviews*, *110*(1-4), 1–25.

Tan, E., & Gurnis, M. (2005). Metastable superplumes and mantle compressibility. *Geophysical Research Letters*, *32*(20).

Tan, E., Leng, W., Zhong, S., & Gurnis, M. (2011). On the location of plumes and lateral movement of thermochemical structures with high bulk modulus in the 3-d compressible mantle. *Geochemistry, Geophysics, Geosystems*, *12*(7).

Tolstikhin, I., & Hofmann, A. W. (2005). Early crust on top of the Earth's core. *Physics of the Earth and Planetary Interiors*, *148*(2-4), 109–130.

Trampert, J., Deschamps, F., Resovsky, J., & Yuen, D. (2004). Probabilistic tomography maps chemical heterogeneities throughout the lower mantle. *Science*, *306*(5697), 853–856.

Tucker, J. M., van Keken, P. E., & Ballentine, C. J. (2022). Earth's missing argon paradox resolved by recycling of oceanic crust. *Nature Geoscience*, 1–6.

Valentine, A. P., & Davies, D. R. (2020). Global models from sparse data: A robust estimate of Earth's residual topography spectrum. *Geochemistry, Geophysics, Geosystems*, *21*(8), e2020GC009240.

Vilella, K., Bodin, T., Boukaré, C.-E., Deschamps, F., Badro, J., Ballmer, M. D., & Li, Y. (2021). Constraints on the composition and temperature of llsvps from seismic properties of lower mantle minerals. *Earth and Planetary Science Letters*, *554*, 116685.

Walter, M. J. (1998). Melting of garnet peridotite and the origin of komatiite and depleted lithosphere. *Journal of Petrology*, *39*(1), 29–60.

Ward, J., Nowacki, A., & Rost, S. (2020). Lateral Velocity Gradients in the African Lower Mantle Inferred From Slowness Space Observations of Multipathing. *Geochemistry, Geophysics, Geosystems*, *21*(8), e2020GC009025. doi: 10.1029/2020GC009025

Watkins, C. E., & Conrad, C. P. (2018). Constraints on dynamic topography from asymmetric subsidence of the mid-ocean ridges. *Earth and Planetary Science Letters*, *484*, 264–275. doi: 10.1016/j.epsl.2017.12.028

White, W. M. (2015). Isotopes, dupal, llsvps, and anekantavada. *Chemical Geology*, *419*, 10–28.

Widmer, R., Masters, G., & Gilbert, F. (1992). Observably split multiplets—data analysis and interpretation in terms of large-scale aspherical structure. *Geophysical Journal International*, *111*(3), 559–576.

Woodhouse, J. (1980). The coupling and attenuation of nearly resonant multiplets in the Earth's free oscillation spectrum. *Geophysical Journal International*, *61*(2), 261–283.

Workman, R. K., & Hart, S. R. (2005). Major and trace element composition of the depleted MORB mantle (DMM). *Earth and Planetary Science Letters*, *231*(1-2), 53–72.

Yang, T., & Gurnis, M. (2016). Dynamic topography, gravity and the role of lateral viscosity variations from inversion of global mantle flow. *Geophysical Journal International*, *207*(2), 1186–1202. doi: 10.1093/gji/ggw335

Zega, T. J., Garvie, L. A., & Buseck, P. R. (2003). Nanometer-scale measurements of iron oxidation states of cronstedtite from primitive meteorites. *American Mineralogist*, *88*(7),

1169–1172.
Zhang, H., Hirschmann, M., Cottrell, E., & Withers, A. (2017). Effect of pressure on fe3+/σfe ratio in a mafic magma and consequences for magma ocean redox gradients. *Geochimica et Cosmochimica Acta*, *204*, 83–103.
Zhong, S., & Hager, B. H. (2003). Entrainment of a dense layer by thermal plumes. *Geophysical Journal International*, *154*(3), 666–676.